Enhanced Sensorless Control of Switched Reluctance Motors Using Inertial Phase-locked Loop for Extended Speed Range

Zifeng Chen, Xijian Lin, Huayu Ji, *Student Member, IEEE*, Zehua Li, Hang Zhao, *Member, IEEE*, and Dianxun Xiao, *Member, IEEE*

***Abstract*—Sensorless control of switched reluctance motors (SRMs) often requires a hybrid mode combining low-speed pulse injection methods and high-speed model-based estimation. However, pulse injection causes unwanted audible noises and torque ripples. This article proposes an enhanced model-based sensorless approach to extend downwards the speed range in which sensorless control can work without injection. An inertial phase-locked loop (IPLL) based on a stator flux observer is introduced for position estimation. Compared to the conventional phase-locked loop scheme, the IPLL offers a more robust disturbance rejection capability and thus reduces the flux model errors at lower speeds. Experimental results substantiate the feasibility of the extended low-speed operation using the model-based sensorless control approach.**

***Index Terms*—Inertial phase-locked loop, Switched reluctance motor, Sensorless control.**

I. Introduction

IN recent years, switched reluctance motors (SRMs) have emerged as prominent contenders in high-speed, high-temperature, and high-reliability applications due to their advantages of simple structure, robustness, and low cost. Industries such as industrial high-power traction motors, transportation electrification, and aerospace [1]-[5] have benefited from these attributes. Conventional position sensors such as resolvers, encoders, and hall sensors play a crucial role in enabling precise control of SRMs by capturing accurate positional information. However, these sensors not only increase system costs and volume but are also susceptible to interference, especially in harsh operating conditions, thereby reducing overall system reliability. Therefore, research on sensorless control strategies is essential for enhancing the performance of SRM systems. Current sensorless control methods primarily include injection methods [6]-[11] and non-injection methods [12]-[20].

The injection method is commonly employed for applications in the low-speed range. The core of this approach involves injecting additional high-frequency pulse voltages into the motor's inactive phases [6]-[11]. This injection allows for the observation of magnetic flux variations, thereby providing accurate information on rotor position and speed. [8] and [9] demonstrate that injecting current pulses into inactive phases effectively detects rotor position, triggering commutation when the peak current injection exceeds a specific threshold. However, sensorless control schemes based on pulse injection are not suitable for high-speed motor operations. This limitation arises because increasing rotor speed shortens the idle phase duration, thereby reducing the accuracy of position estimation using most pulse injection methods. Moreover, pulse injection can introduce high-frequency noise and electromagnetic compatibility issues [11].

Non-injection schemes are often employed in the high-speed operation range of motors. At high speeds, SRMs exhibit large back electromotive force (back EMF) and higher signal-to-noise ratio (SNR). Therefore, more accurate position estimation can be achieved by monitoring magnetic characteristics. For instance, full position estimation is achieved using special position flux linkage methods [12]-[13]. Also, this includes rotor position and speed prediction via current gradient [14] and inductance gradient methods [15]-[16]. Additionally, state observer-based approaches are focused on sensorless control research. [17] proposed a nonlinear observer combined with flux linkage characteristics for rotor position prediction. [18] proposed a sensorless control scheme based on a single-phase adaptive observer,

Manuscript received November 14, 2024; revised January 09, and February 24, 2025; accepted March 31, 2025. Date of publication June 25, 2025; Date of current version April 28, 2025.

This work was supported in part by the National Natural Science Foundation of China 52307069, in part by 2024 Tertiary Education Scientific Research Project of Guangzhou Municipal Education Bureau under Grant 2024312176, and in part by the Project of Hetao Shenzhen-Hong Kong Science and Technology Innovation Cooperation Zone under Grant HZQB-KCZYB-2020083. (*Corresponding author*: *Dianxun Xiao*)

Dianxun Xiao is with the Sustainable Energy and Environment Thrust, The Hong Kong University of Science and Technology (Guangzhou), Guangzhou 511453, China, The Hong Kong University of Science and Technology, Clear Water Bay, HKSAR, China, and also with the HKUST Shenzhen–Hong Kong Collaborative Innovation Research Institute, Shenzhen 518048, China (e-mail: dianxunxiao@hkust-gz.edu.cn).

Zifeng Chen is with Sustainable Energy and Environment Thrust, The Hong Kong University of Science and Technology (Guangzhou), Guangzhou, 511453, China, and The Hong Kong University of Science and Technology, Clear Water Bay, HKSAR, China.

Xijian Lin, Huayu Ji, and Zehua Li are with Sustainable Energy and Environment Thrust, The Hong Kong University of Science and Technology (Guangzhou), Guangzhou, 511453, China.

Hang Zhao is with the Robotics and Autonomous Systems Thrust, Systems Hub, The Hong Kong University of Science and Technology (Guangzhou), Guangzhou 511453, China.

Digital Object Identifier 10.30941/CESTEMS.2025.00013

achieving position estimation by reducing magnetic nonlinearity and compensating for angular errors. However, this approach exhibits poor dynamic performance due to the limitations of the single-phase observer's filtering capability. Building upon this, the work in [19] introduced a multi-stage cascaded delay factor method to better eliminate harmonics within the flux linkage, further enhancing sensorless dynamic performance. Nonetheless, this method demands substantial computational resources, making it less suitable for cost-sensitive applications. [20] combines direct computation methods with flux observers. Initially, rotor position estimation is achieved through numerical methods and a three phase phase-locked loop (PLL), leveraging relationships between position, phase currents, and flux linkages. As noted in [17]-[20], most model-based methods face challenges at low speeds due to the accumulation of integration errors in flux linkage calculations. This limitation means that these sensorless control schemes can only be effectively applied to the high-speed range of the motor. To address these issues, a hybrid sensorless control strategy that combines pulse injection and model-based methods is often required. However, as pointed out in references [21]-[22], this approach introduces additional noise and torque ripples at low speeds due to pulse injection. These drawbacks further constrain the widespread adoption of sensorless control.

Therefore, extending the minimum speed range of model-based methods is crucial to reduce the time using pulse injection. To this end, the paper proposes an enhanced sensorless control scheme based on an inertial phase-locked loop (IPLL). The main contributions of this paper are summarized as follows:

1) Addressing the issue of cumulative error in flux calculation at low to medium speeds, the IPLL scheme extends the speed range. Compared to conventional methods [20], it maintains good estimation accuracy and control effectiveness at lower speeds.

2) The proposed scheme avoids complex computations and enhances the understanding of the system's dynamic behavior through time-domain analysis, laying a solid foundation for subsequent system optimization and control.

The working principles, characteristics, and design methodology of the proposed IPLL are analyzed in detail. Experimental tests on a 12/8 SRM setup prove the effectiveness of the low-speed extension.

II. SRM Sensorless Drive and Position Estimation Scheme

A. SRM Sensorless Drive System

Fig. 1 depicts the sensorless three-phase 12/8 SRM drive system, which comprises several components: a three-phase asymmetric half-bridge converter (AHBC), current sensors, a microcontroller unit (MCU), six gate drivers for insulated gate bipolar transistor (IGBT), and power supply. The function of the AHBC is to regulate the bipolar voltage to generate the unipolar current required by the SRM, ensuring that each phase can be independently controlled. The gate driver is responsible for providing gate signals for the semiconductor switches, which are generated within the control board based on references of speed, current, or torque. The AHBC incorporates three distinct switching modes for each phase, as delineated in Fig. 2. The first mode, termed the magnetization mode, is initiated when both switches are concurrently turned on, as depicted in Fig. 2(a). The stator is subjected to the direct current (DC) link voltage, denoted as $+U_{dc}$, leading to an augmentation in the stator current. The second mode, illustrated in Fig. 2(b) and referred to as the demagnetization mode, is activated when both switches are simultaneously turned off. This configuration imposes a negative phase voltage, $-U_{dc}$, on the windings, thereby inducing demagnetization and facilitating the return of the energy accumulated in the windings to the DC bus. The final mode, represented in Fig. 2(c), is the freewheeling mode. In this mode, one switch remains deactivated while the other is activated, permitting current circulation solely at the zero-phase voltage juncture. Following precise rotor position and speed signal acquisition through sensorless control algorithms, the drive system implements proportional-integral (PI)-based speed control and current hysteresis control. Ultimately, the on/off signals are output to the AHBC to achieve precise control of the SRM.

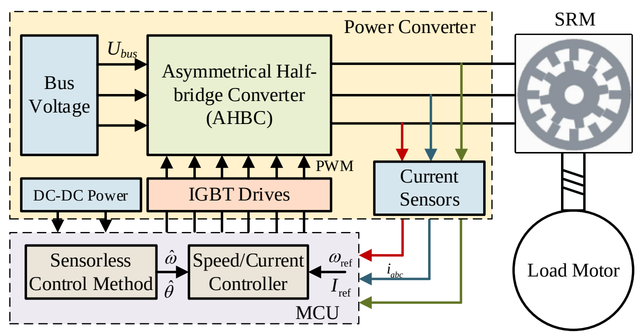

Fig. 1. The control diagram of the three-phase 12/8 SRM sensorless drive.

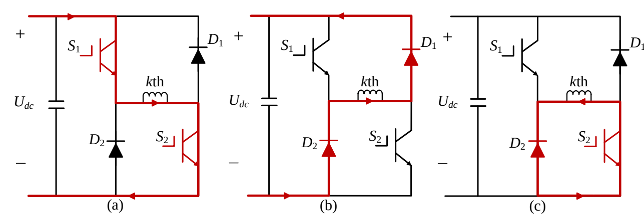

Fig. 2. Switching operating modes of the asymmetrical half-bridge converter. (a) Magnetization. (b) Demagnetization. (c) Freewheeling.

B. The Model of SRM and Position Estimation

According to Kirchhoff's law, the voltage balance equation of SRM can be expressed as:

$$u = R_s i + \frac{\mathrm{d}\Psi(\theta, i)}{\mathrm{d}t} \tag{1}$$

where u, i, and R_s respectively denote the phase voltage, phase current, and winding resistance of the phase winding. The flux linkage Ψ of the phase winding is a nonlinear function of the phase current i and the rotor position angle θ. Fig. 3 shows the flux linkage distribution of the three-phase 5.5 kW 12/8 SRM. The currents are measured by current sensors, and for the unknown θ, Ψ can be initially measured by integrating (1):

$$\Psi(\theta,i)=\int\left(u-R_s i\right)\mathrm{d}t \tag{2}$$

Given that $\Psi(\theta, i)$ varies with both θ and i, within a localized region surrounding a specific point in Fig. 3.

$$\Delta\Psi=\left.\frac{\partial\Psi}{\partial i}\right|_{\theta=\mathrm{const}}\Delta i+\left.\frac{\partial\Psi}{\partial\theta}\right|_{i=\mathrm{const}}\Delta\theta \tag{3}$$

Since the current can be directly measured, setting Δi to zero allows to express (3) as:

$$\theta-\hat{\theta}=\left.\frac{\partial\theta}{\partial\Psi}\right|_{i=\mathrm{const}}(\Psi-\hat{\Psi}) \tag{4}$$

where $\hat{\theta}$ denotes the estimated rotor position close to its actual location, and $\hat{\Psi}$ represents the estimated flux linkage associated with it. By deducting the flux linkage estimate $\hat{\Psi}$, derived using the lookup table approach, from the calculated flux linkage Ψ, the position error e is determined through the conversion of magnetic characteristics as outlined in (4).

$$e=\theta-\hat{\theta}=g(\Psi-\hat{\Psi}) \tag{5}$$

where $g=\dfrac{\partial\theta}{\partial\Psi}$, is the partial derivative of θ with respect to Ψ, aiming to convert flux linkage error into position error and the value of g varies with the change in phase current. For simplicity in calculations, only the minimum values at different currents are considered, and the values of g at different currents are plotted using multi-parameter polynomial fitting, as shown in Fig. 4.

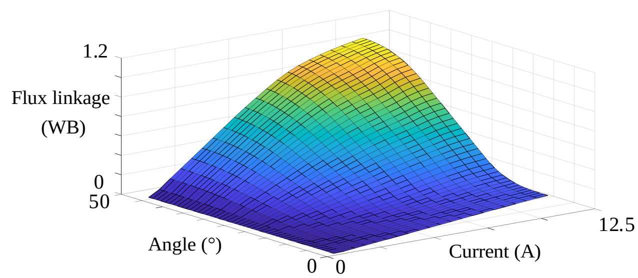

Fig. 3. Flux linkage profile of the studied SRM.

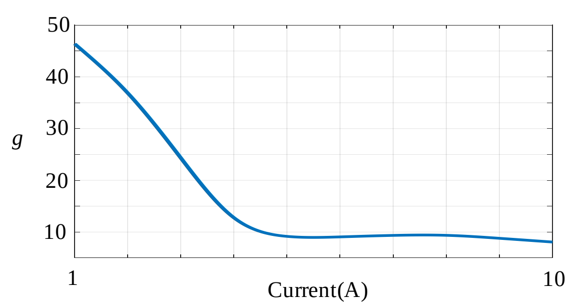

Fig. 4. The value of g under different current.

Although smaller gains could result in a slow convergence speed, this approach does not lead to large errors and does not affect the stability of the system. Based on (5), the position error can be calculated, making the use of a three-phase PLL to converge the position error and compute the rotor's speed and position an efficient approach [20]. However, due to the presence of an integrator within the PLL, this scheme tends to accumulate integral errors at low speeds, rendering the three-phase PLL approach unsuitable at low velocities. Consequently, to enhance the versatility of sensorless control, it is imperative to improve the reliability and estimation accuracy of sensorless control strategies at medium/low speeds without injection signals.

III. Design and Analysis of IPLL-based Sensorless Control Approach

To address the reliability and estimation accuracy issues of the non-injection scheme discussed in Section II, this chapter upgrades the conventional three-phase PLL and introduces a sensorless control scheme based on an IPLL.

A. The Analysis of the Typical PLL

Fig. 5 depicts the configuration of a conventional PLL, where $\hat{\omega}$ denotes the estimated speed obtained from the PLL. Moreover, the loop transfer function of the PLL from $\hat{\omega}$ to e is represented as:

$$G_{\mathrm{PLL}}(s)=\frac{\hat{\omega}}{e}=k_{\mathrm{p}}+\frac{k_{\mathrm{i}}}{s} \tag{6}$$

The physical significance of the transfer function $G_{\mathrm{PLL}}(s)$ lies in its representation of how estimation errors caused by factors such as sensor noise, computational inaccuracies, and model uncertainties affect estimation speed. When the gain of the transfer function is high, it indicates that estimation errors have a significant impact on estimation speed, resulting in lower system accuracy. Conversely, when the gain is low, it suggests that the system is capable of suppressing estimation errors, thereby enhancing the accuracy of estimation speed.

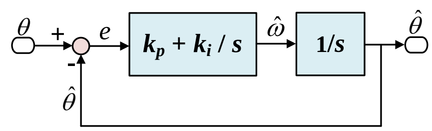

Fig. 5. The block diagram of the conventional PLL.

Fig. 6 shows the unit step response of the system under varying control parameters for $G_{\mathrm{PLL}}(s)$. Fig. 6(a) illustrates the effect of the control parameter k_{p} on the system's unit step response. As the proportional gain k_{p} increases, the system's response speed accelerates, allowing it to approach the steady-state value more quickly. However, due to the integral action, the output exhibits a trend of linear increase, which may lead to an overshoot or peak. Additionally, the initial value of the unit step response changes with variations in k_{p} because the proportional gain term generates an initial output at t=0 that is equal to the value of k_{p}. The impact of control parameters on k_{i}, as shown in Fig. 6(b), is such that the initial value of the unit step response remains constant, but the response speed increases nonlinearly with an increase in k_{i}. This means that increasing k_{i} can accelerate the system's response speed, but the initial state is unaffected. Moreover, when the PLL is stable, the input e=0 and the estimated speed $\hat{\omega}$ equals the actual real speed. This is also the working principle of the PLL, which ensures the stable operation of the system by locking the phase.

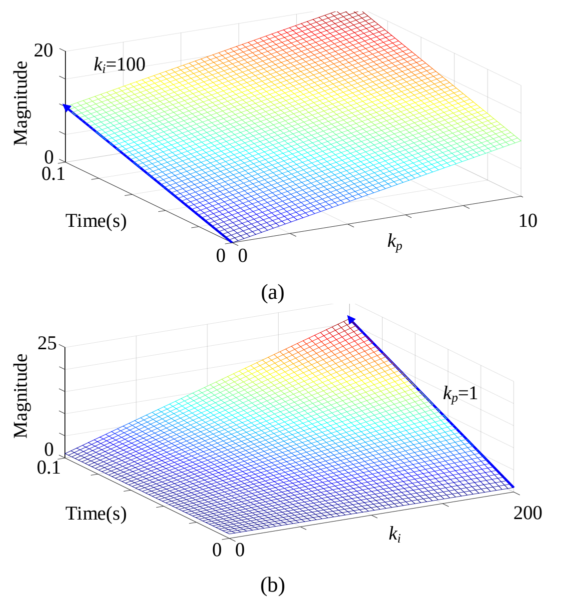

Fig. 6. The unit-step responses of the conventional PLL with various control parameters. (a) k_i=100. (b) k_p=1.

In addition, from Fig. 5, the estimated rotor position $\hat{\theta}$ can be obtained as:

$$\hat{\theta} = \int \hat{\omega} \mathrm{d}t \tag{7}$$

The closed-loop transfer function $G_{\mathrm{PLLc}}(s)$ of the conventional PLL from input to output is represented as:

$$G_{\mathrm{PLLc}}(s) == \frac{\hat{\theta}}{\theta} = \frac{k_{\mathrm{p}}s + k_{\mathrm{i}}}{s^2 + k_{\mathrm{p}}s + k_{\mathrm{i}}} \tag{8}$$

The Bode plot of (8) is shown in Fig. 7. As the bandwidth increases, the PLL is able to track the target frequency more quickly, thereby improving dynamic performance. Besides, the Bode plot shows that the gain in the mid-frequency range is greater than zero, indicating that the observed values in this range are biased high, which can easily lead to oscillations. The increase in bandwidth also makes the PLL more susceptible to high-frequency disturbances, potentially causing oscillation and reducing the stability of the system.

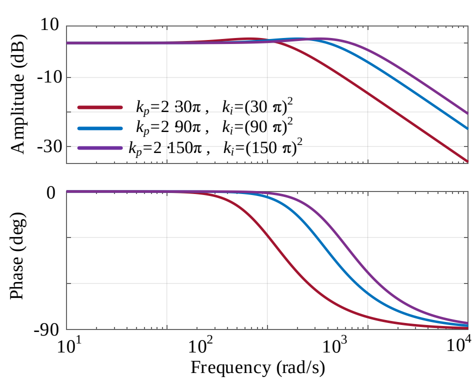

Fig. 7. The Bode plot of the conventional PLL under different bandwidths.

B. The Analysis of the Proposed IPLL-based Position Observer

To address the issue of inaccurate estimation of conventional PLL at medium/low speeds as analyzed in the previous section, this paper uses an IPLL for sensorless control of an SRM. Prior to this, the IPLL is used to address the issue of sub-synchronous resonance (SSR) when renewable energy generation systems are integrated into weak grids [23]-[24]. The design process of IPLL is as follows in Fig. 8. Fig. 8 illustrates the block diagram of the IPLL, where $\hat{\omega}$ denotes the estimated speed, ω_{ref} is the speed reference value, and $\hat{\theta}$ stands for the estimated position. The open loop transfer function of the IPLL from $\hat{\omega}$ to e is given by (9).

$$G_{\mathrm{IPLL}}(s) = \frac{\hat{\omega}}{e} = \frac{A_{\mathrm{k}}}{s + A_{\mathrm{k}}A_{\mathrm{p}}} \tag{9}$$

where A_{k} and A_{p} represent the inertia control parameters. The estimated angle $\hat{\theta}$ can also be obtained according to (7). Fig. 9 illustrates the step response of the IPLL-based system under varying parameters. This figure shows that as A_{k} increases, the transition time decreases. Additionally, the steady-state amplitude of the step response corresponds to the derivative of the control parameter A_{p}. As A_{p} increases, the steady-state amplitude of the step response gradually decreases. When the IPLL system reaches a steady state, the following holds:

$$A_{\mathrm{k}}e + A_{\mathrm{p}}(\omega_{\mathrm{ref}} - \hat{\omega}) = 0 \tag{10}$$

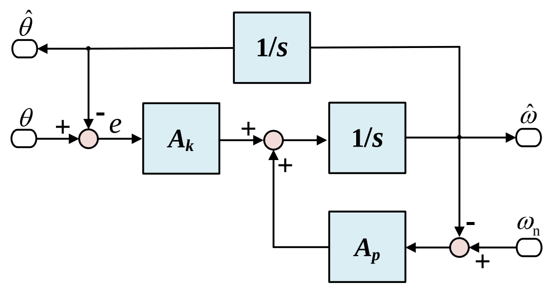

Fig. 8. The block diagram of the proposed IPLL.

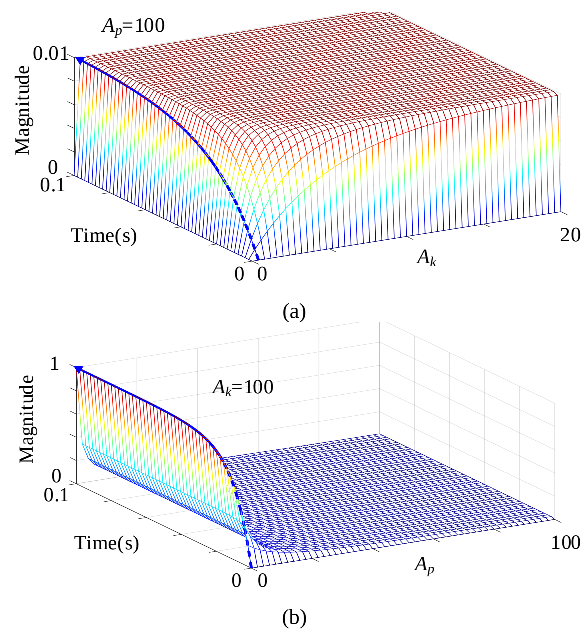

Fig. 9. The unit-step responses of the proposed IPLL with various control parameters. (a) A_{p} = 100. (b) A_{k} = 100.

Based on (9), the error e can be expressed as:

$$e=\frac{A_{\mathrm{p}}(\hat{\omega}-\omega_{\mathrm{n}})}{A_{\mathrm{k}}} \tag{11}$$

According to Fig. 10, the closed-loop transfer function of the IPLL can be expressed as:

$$G_{\mathrm{IPLLc}}(s)=\frac{\hat{\theta}}{\theta}=\frac{A_{\mathrm{k}}}{s^2+A_{\mathrm{p}}s+A_{\mathrm{k}}} \tag{12}$$

The Bode plot for (12) is shown in Fig. 10. As A_{k} and A_{p} increase, although the high-frequency noise suppression capability of the IPLL for the system decreases, it demonstrates improved tracking ability for the instantaneous changes of the input signal as the phase delay reduces. Therefore, when adjusting the IPLL system's parameters, a balance must be struck between dynamic response, noises, and system stability, selecting the appropriate bandwidth based on design requirements to achieve better effects.

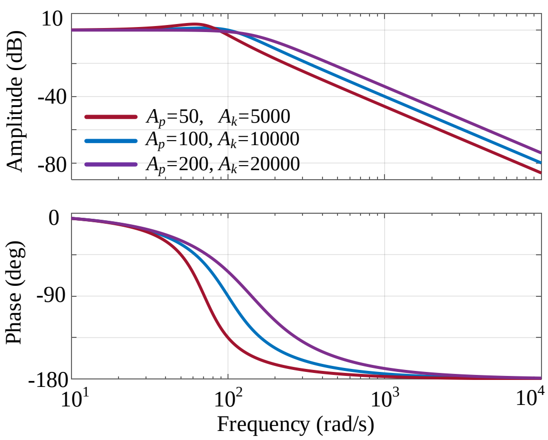

Fig. 10. The Bode plot of the IPLL under different bandwidths.

C. Comparative between the PLL and the Proposed IPLL

This section offers a comprehensive comparison between the conventional PLL and the proposed IPLL, analyzing their performance under conditions of same bandwidth and identical parameters.

To further enhance this comparison and better understand the performance differences, the Bode plots of the proposed IPLL and the PLL are compared with the same bandwidth, as shown in Fig. 11. From Fig. 11, it can be seen that when the bandwidths of the PLL and IPLL are consistent, the IPLL exhibits stronger noise suppression capabilities in the low to high-frequency range, making it less susceptible to interference and thereby improving estimation accuracy. For example, at a frequency of 10^3 rad/s, the amplitude of IPLL is -40 dB, while the amplitude of PLL is approximately -20 dB, indicating that the noise suppression capability of IPLL is 10 times that of PLL. Based on the above analysis, the proposed IPLL method has better steady-state estimation accuracy and stability compared to the conventional PLL method.

Moreover, by observing the closed-loop transfer function expressions (8) and (12) of PLL and IPLL, it can be found that IPLL is a typical second-order system, while PLL has an additional zero based on the typical second-order system. Therefore, the closed-loop transfer functions of PLL and IPLL can be equivalently represented respectively as follows.

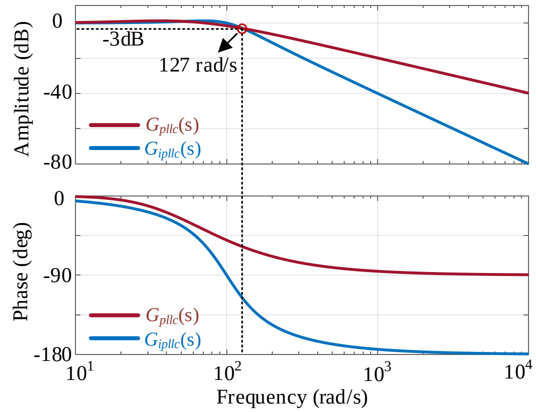

Fig. 11. Comparison of Bode plots for PLL and proposed IPLL with the same bandwidth.

$$M_{\mathrm{PLLc}}(s)=\frac{\omega_{\mathrm{n}}^2(1+T_{\mathrm{z}}s)}{s^2+2\zeta\omega_{\mathrm{n}}s+\omega_{\mathrm{n}}^2} \tag{13}$$

$$M_{\mathrm{IPLLc}}(s)=\frac{\omega_{\mathrm{n}}^2}{s^2+2\zeta\omega_{\mathrm{n}}s+\omega_{\mathrm{n}}^2} \tag{14}$$

Among them, ω_{n} represents the natural frequency and ζ represents the damping ratio. For equation (13), $k_{\mathrm{p}}=2\zeta\omega_{\mathrm{n}}$ and $k_{\mathrm{i}}=\omega_{\mathrm{n}}^2$. For equation (14), $\mathrm{A_p}=2\zeta\omega_{\mathrm{n}}$ and $\mathrm{A_k}=\omega_{\mathrm{n}}^2$. Therefore, the closed-loop zero of equation (13) is:

$$s=-\frac{1}{T_{\mathrm{z}}}=-\frac{k_{\mathrm{i}}}{k_{\mathrm{p}}} \tag{15}$$

As the value of T_{z} increases, the value of the zero gradually decreases, which causes the closed-loop zero s to approach the origin in the complex plane. Decompose (13) into the following form for further analysis:

$$\begin{aligned}M_{\mathrm{PLLc}}(s)&=M_{\mathrm{IPLLc}}(s)+\frac{\omega_{\mathrm{n}}^2T_{\mathrm{z}}s}{s^2+2\zeta\omega_{\mathrm{n}}s+\omega_{\mathrm{n}}^2}\\&=\frac{\omega_{\mathrm{n}}^2}{s^2+2\zeta\omega_{\mathrm{n}}s+\omega_{\mathrm{n}}^2}+\frac{\omega_{\mathrm{n}}^2T_{\mathrm{z}}s}{s^2+2\zeta\omega_{\mathrm{n}}s+\omega_{\mathrm{n}}^2}\end{aligned} \tag{16}$$

When the input signal is a unit step signal, the output corresponding to the first term $M_{\mathrm{IPLLc}}(s)$ of (16) is $y_{\mathrm{IPLLc}}(t)$, and the unit step response of the PLL can be expressed as:

$$y_{\mathrm{PLL}}(t)=y_{\mathrm{IPLL}}(t)+T_{\mathrm{z}}\frac{\mathrm{d}y_{\mathrm{IPLL}}(t)}{\mathrm{d}t} \tag{17}$$

Based on (17), Fig. 12 shows the unit step responses of IPLL and PLL under the same parameter conditions. It can be observed from the figure that as IPLL does not contain a zero point, during the step response process, the maximum overshoot of IPLL is effectively controlled compared to PLL, reducing from the original 29.8% to 16.3%. Meanwhile, although the settling time t_{s} of IPLL has slightly increased by 0.005 s, compared to the overall response process, this increment is almost negligible and has a minor impact on the system.

In the field of sensorless control, excessive overshoot has an impact on the accuracy of position estimation. Specifically, overshoot increases the deviation in rotor position estimation, and the rotor position directly determines the commutation timing of the SRM. Once the angle deviation is too large, the commutation timing is disrupted and cannot proceed in an orderly manner, which affects the accuracy of torque output and weakens the smoothness and efficiency of motor operation. In summary, under the same parameters, IPLL demonstrates superior transient performance compared to PLL, with a 45% reduction in maximum overshoot.

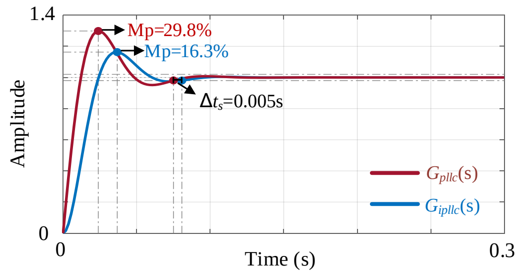

Fig. 12. Comparison of unit step responses between IPLL and proposed PLL with the same parameters.

D. Overview of the Sensorless Control Scheme based on the Proposed IPLL

The proposed SRM drive employs a sensorless technique based on IPLL to estimate the SRM's position and speed. The estimated position and speed information are used for speed and position feedback. Fig. 13 provides a detailed illustration of the implementation process of sensorless control, where the core steps include the calculation of flux linkage, acquisition of flux linkage error, and the estimation of speed and position based on IPLL. Initially, Ψ is calculated through real-time monitoring of the SRM's current and voltage. Concurrently, the expected flux linkage $\hat{\Psi}$, is obtained via a lookup table method, which is pre-set according to the motor's known magnetic characteristics. Then, by subtracting Ψ from $\hat{\Psi}$, the flux linkage error is calculated. This step is crucial for the flux linkage error directly affects the accurate acquisition of position error e, which is derived using the transformation of magnetic characteristics formula based on (4). Subsequently, the flux linkage error is processed using IPLL to estimate the speed and position. The IPLL is a closed-loop feedback system, which adjusts its phase according to the input position error to lock onto the motor's actual speed and position. The advantage of this method is that through dynamic adjustment, IPLL can effectively compensate for errors caused by load variations or external disturbances, thereby ensuring the accuracy and stability of control.

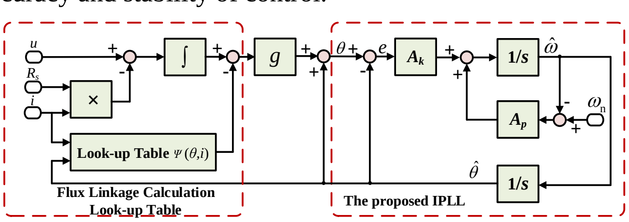

Fig. 13. Block diagram of the IPLL for the SRM sensorless control.

As pointed out in the analysis in Section C, compared to the conventional PLL, the IPLL exhibits stronger robustness to disturbances while the bandwidth remains the same. It means the position estimation accuracy can be enhanced under a noisier condition. This enables the sensorless control strategy to operate effectively across a broader speed range, especially in the mid to low-speed range, which is crucial for achieving efficient and high-performance motor control.

IV. Experimental Results and Analysis

Experiments are conducted on the three-phase 5.5 kW 12/8 SRM experimental setup to evaluate the proposed position sensorless control strategy. The setup, shown in Fig. 14, includes the SRM, a load asynchronous induction motor (IM) connected via a flexible coupling, and a power converter with an asymmetrical half-bridge circuit using IGBTs (model IGW60T120) and Schottky diodes (model D100E60). The sensorless algorithm tests were carried out on a TMS320F28335 control board, with phase currents regulated through A/D conversion and PWM. The sampling frequency is set at 20 kHz. The phase resistance of SRM is 1.29 Ω, with turn-on and turn-off angles of 0° and 20° respectively. The parameters of IPLL are set to A_k=100 and A_p=10000 to achieve a balanced combination of harmonic suppression and response speed. According to [11], [18], the PI parameters in conventional PLL can be configured as $k_p=2\omega_{PLL}$ and $k_i=\omega_{PLL}^2$, with the bandwidth of ω_{PLL}=251.2. All tests are conducted in sensorless control mode, with estimated position and speed as feedback for the control loop. Experimental results are obtained based on a TekMDO34 oscilloscope.

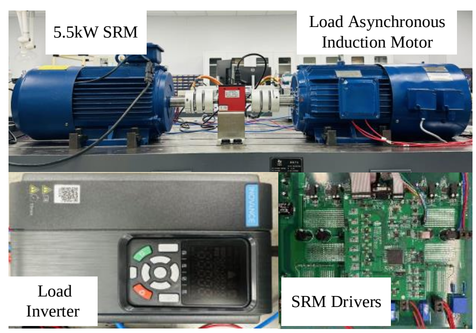

Fig. 14. Three-phase 12/8 SRM experimental setup.

Fig. 15(a) shows a comparison between the calculated flux linkage Ψ and the flux linkage $\hat{\Psi}$ obtained by the lookup table method at 300 r/min, indicating a similarity in the values of flux linkage obtained by the two methods. Fig. 15(b) displays the current waveform of phase A, with chopping current control selected as the control method. As can be observed, the flux linkage calculated online has a mismatch with the lookup table. This phenomenon is caused by measurement noises and disturbances, particularly at low speeds where the flux linkage becomes lower.

Fig. 16(a), (b), (c), and (d) respectively show the steady-state position error and real/estimated position comparison of the proposed sensorless control scheme based on IPLL at 200 r/min, 300 r/min, 400 r/min, and 500 r/min. It can be observed that at 200 r/min, the maximum position error is 2.7°. At 300 r/min, the maximum position error is approximately 2.0°. At 400 r/min, the maximum position error is around 1.8°. At

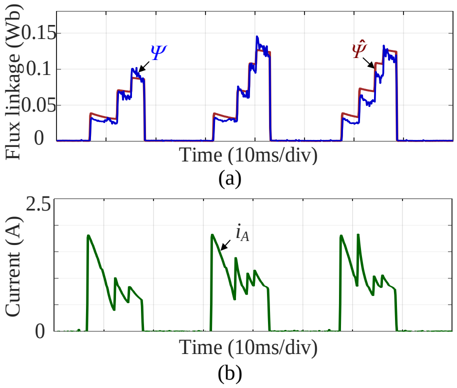

Fig. 15. Experimental results of flux linkage and current at 300r/min. (a) Comparison between calculated flux linkage Ψ and lookup table flux linkage $\hat{\Psi}$. (b) Phase current.

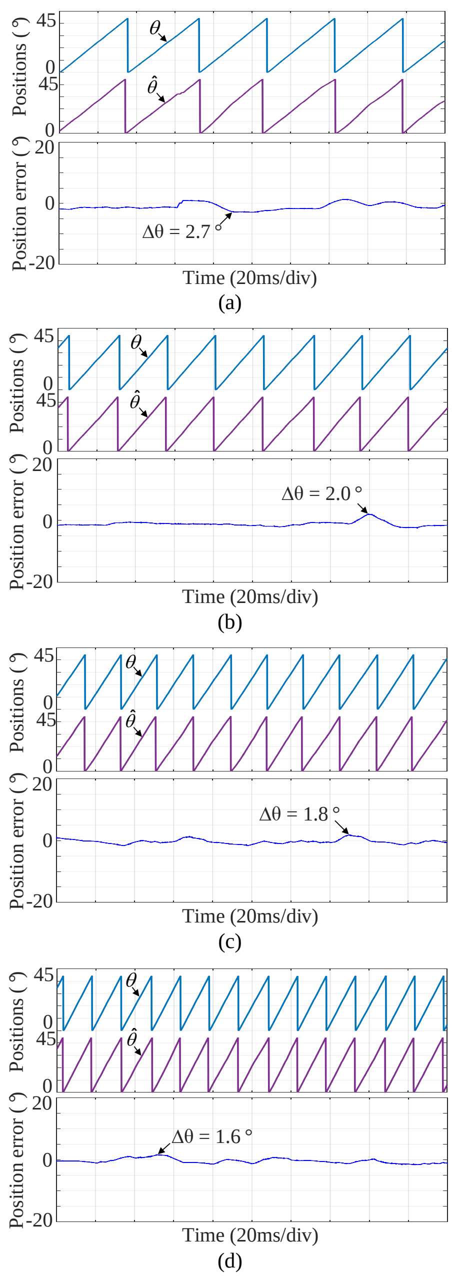

Fig. 16. Position estimation results of the proposed sensorless method. (a) 200 r/min. (b) 300 r/min. (c) 400 r/min. (d) 500 r/min.

500 r/min, the maximum position error is about 1.6°. It is evident that the estimated position can track the real position under different speed conditions and the estimation accuracy improves with increasing speed.

To better validate the effectiveness of the proposed IPLL sensorless control scheme, a set of comparative experiments are conducted, as shown in Fig. 17. Fig. 17(a), (b), (c), and (d) depict the steady-state position error and position comparison of the conventional PLL sensorless control scheme at 200 r/min, 300 r/min, 400 r/min, and 500 r/min. As illustrated in Fig. 17(a), at 200 r/min, the estimated position fails to track the actual position, resulting in ineffective sensorless control. Under operating conditions of 300 r/min, 400 r/min, and 500 r/min, the estimated position can track the actual position,

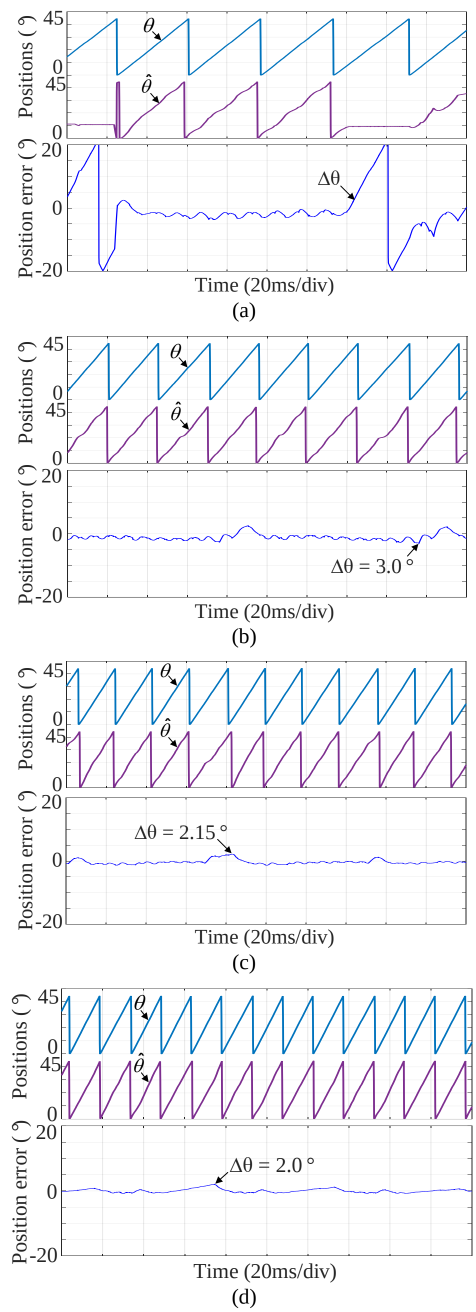

Fig. 17. Position estimation results of the conventional PLL sensorless method. (a) 200 r/min. (b) 300 r/min. (c) 400 r/min. (d) 500 r/min.

with steady-state errors of 3°, 2.15°, and 2°, respectively. It can be observed that as the speed increases, the steady-state position error continues to decrease. Compared to the proposed IPLL scheme, the conventional PLL-based sensorless control scheme exhibits higher steady-state errors, particularly evident in the lower speed range (such as 200 r/min and 300 r/min).

To summarize and present the data from Fig. 16 and Fig. 17 in a more concise and quantitative way, Table I is added. This table quantitatively compares the position errors between the proposed IPLL and conventional PLL methods at different speeds. For the proposed IPLL method, as the rotor speed increases from 200 r/min to 500 r/min, the position error decreases from 2.7° to 1.6°, indicating improved accuracy with higher speeds. In contrast, the conventional PLL method fails at 200 r/min. At 300 r/min, 400 r/min, and 500 r/min, its position errors are 3.0°, 2.15°, and 2.0° respectively. Clearly, the proposed IPLL method outperforms the conventional PLL method in terms of position error, further validating the effectiveness of the proposed sensorless control scheme.

TABLE I
QUANTITATIVE COMPARISON OF POSITION ERRORS BETWEEN PROPOSED IPLL AND CONVENTIONAL PLL METHODS AT DIFFERENT SPEEDS

Rotor speed (r/min)	Method	Position error (°)
200	Proposed IPLL	2.7
300	Proposed IPLL	2.0
400	Proposed IPLL	1.8
500	Proposed IPLL	1.6
200	Conventional PLL	Fail
300	Conventional PLL	3.0
400	Conventional PLL	2.15
500	Conventional PLL	2.0

Figs. 18 and 19 illustrate the speed tracking performance test results of the proposed IPLL scheme compared to the conventional PLL scheme at 250 r/min and 500 r/min, respectively. The test results indicate that the sensorless control scheme based on IPLL exhibits advantages in terms of speed ripple, with the amplitude of the speed ripple being lower than that of the conventional control scheme. This phenomenon is validated under both 250 r/min and 500 r/min operating conditions, demonstrating the proposed IPLL scheme's superiority in speed stability.

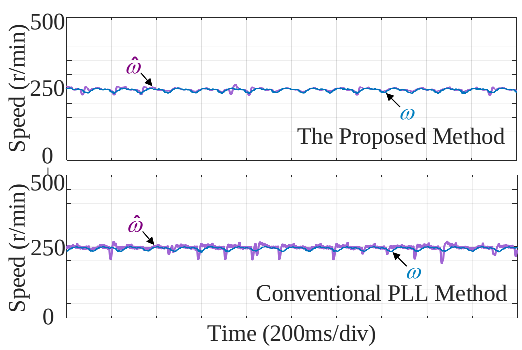

Fig. 18. The comparison experiment of steady-state speed tracking performance at 250 r/min.

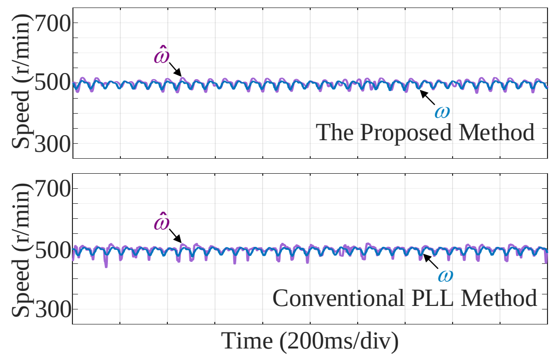

Fig. 19. The comparison experiment of steady-state speed tracking performance at 500 r/min.

Besides, Table II is introduced for a quantitative analysis. This table systematically presents numerical data on the peak speed errors of the proposed IPLL and conventional PLL methods at 250 r/min and 500 r/min. For the IPLL method, the peak speed errors are recorded as 22 r/min at 250 r/min and 24 r/min at 500 r/min. In contrast, the conventional PLL method shows higher values, with 47 r/min at 250 r/min and 62 r/min at 500 r/min. These precise figures not only provide a clear-cut comparison but also offer indisputable evidence of the proposed IPLL scheme's superior speed-tracking performance and enhanced stability, as it consistently yields lower peak speed errors across the tested speeds.

TABLE II
QUANTITATIVE COMPARISON OF SPEED ERRORS BETWEEN PROPOSED IPLL AND CONVENTIONAL PLL METHODS AT DIFFERENT SPEEDS

Rotor speed (r/min)	Method	Peak speed error (r/min)
250	Proposed IPLL	22
500	Proposed IPLL	24
250	Conventional PLL	47
500	Conventional PLL	62

Fig. 20 shows the test of the operating conditions under load disturbance. In this test figure, the comparison between the actual speed and the estimated speed can be clearly seen, and the variation trends of the position error and the phase current are also presented. When the load is suddenly applied, the estimated rotor speed will drop instantaneously, with an amplitude of 92 r/min. However, due to the regulation of the speed controller, the estimated rotor speed is gradually adjusted and finally returns to the reference speed value of 500 r/min. During the unloading process, the estimated rotor speed will increase, also by an amplitude of 90 r/min, and then it will be adjusted back to the reference speed of 500 r/min. It is variation trend of the actual speed, which demonstrates the stability and reliability of its speed tracking ability. Further observation reveals that within the range of loading to the rated current, the position error remains approximately at around 1.2°. During the unloading process, the position error increases, and the maximum position error is approximately 2.0°. In conclusion, from the perspective of the entire test results, even under the operating conditions with load disturbance, the proposed sensorless control algorithm still exhibits robustness.

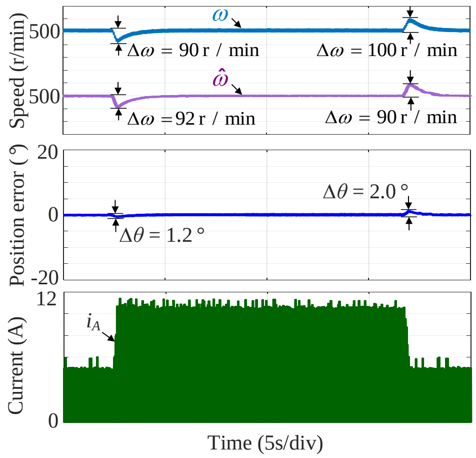

Fig. 20. Position-sensorless control under load change when loading to the rated current at 500 r/min.

Fig. 21 showcases a comparison between the proposed IPLL sensorless control scheme and the conventional PLL sensorless control scheme during a deceleration experiment from 250 r/min to 200 r/min. It is evident in the figure that the IPLL scheme can stably operate in the range from 250 r/min to 200 r/min, whereas the PLL scheme experiences instability under the same conditions. This comparison underscores the advantage of the IPLL scheme in terms of expanded speed capabilities, namely its ability to operate stably at lower speeds, thereby demonstrating enhanced stability and robustness. The experimental results reveal that, in comparison to the conventional PLL scheme, the IPLL sensorless control scheme exhibits superior performance in managing the deceleration process, ensuring stable operation of the motor over a broader speed range.

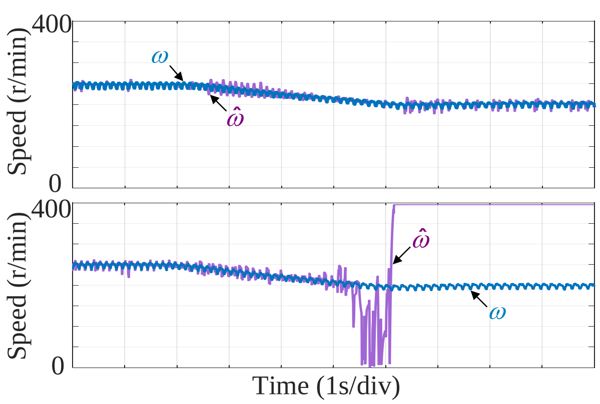

Fig. 21. Comparison of the proposed sensorless scheme and the conventional PLL scheme in the deceleration experiment from 250 r/min to 200 r/min.

V. Conclusion

In this paper, an innovative sensorless control strategy for SRM based on the IPLL is introduced, aiming to overcome the challenges of noise sensitivity and the limitations of conventional observer-based methods that exhibit poor sensorless control accuracy or even failure at low/medium speeds. Compared to conventional methods, the IPLL-based approach features a simpler structure, better steady-state estimation accuracy, and speed control effectiveness, with notably improved performance at low/medium speeds. The effectiveness of the IPLL scheme in extending the operational speed range of SRMs without compromising control precision is further demonstrated through deceleration experiments. In conclusion, the proposed IPLL sensorless control scheme offers a viable solution to the challenges posed by low/mid-speed operations. Its simplicity, enhanced accuracy, and robust performance under various operational conditions suggest that the IPLL sensorless control scheme has a broad application prospect in the SRM field, contributing to the advancement of sensorless control technologies.

References

[1] K. Sreeram, P. K. Preetha, and J. Rodríguez-García *et al*, “A Comprehensive Review of Torque and Speed Control Strategies for Switched Reluctance Motor Drives,” *CES Trans. on Electr. Mach. and Syst.*, vol. 9, no. 1, pp. 46─75, Mar. 2025.

[2] Z. F. Chen, H. Jing, and X. H. Wang *et al*, “High-speed Sensorless Control Strategy of SRMs: Utilizing Fourth Order Generalized Integrator to Enhance Control Performance and Overcome Magnetic Characteristic Constraints,” *IEEE Trans. on Ind. Applicat.*, vol. 61, no. 1, pp. 1─9, Jan.-Feb. 2025.

[3] L. F. Ge, J. X. Zhong, and Q. Y. Cheng *et al*, “Model Predictive Control of Switched Reluctance Machines for Suppressing Torque and Source Current Ripples under Bus Voltage Fluctuation,” *IEEE Trans. on Ind. Electron.*, vol. 70, no. 11, pp. 11013─11021, Nov. 2023.

[4] T. Chen, and G. Y. Cheng, “Comparative Investigation of Torque-ripple Suppression Control Strategies based on Torque-sharing Function for Switched Reluctance Motor,” *CES Trans. on Electr. Mach. and Syst.*, vol. 6, no. 2, pp. 170─178, Jun. 2022.

[5] Z. F. Chen, X. J. Lin, and S. Zhang *et al*, “Torque Ripple Suppression Strategy for Switched Reluctance Motor based on Improved Active Disturbance Rejection Controller,” in *Proc. of 2024 IEEE 7th International Electrical and Energy Conference (CIEEC)*, Harbin, China, 2024, pp. 123─127.

[6] X. Q. Guo, S. G. Zeng, and R. Zhong *et al*, “High-Precision Injection Current Sampling Scheme for Direct Drive Low-speed Position Sensorless Control of Switched Reluctance Machine,” *IEEE Trans. on Ind. Electrons.*, vol. 71, no. 11, pp. 13754─113765, Nov. 2024.

[7] D. X. Xiao, J. Ye, and G. L. Fang *et al*, “Induced Current Reduction in Position-sensorless SRM Drives Using Pulse Injection,” *IEEE Trans. on Ind. Electrons.*, vol. 70, no. 5, pp. 4620─4630, May 2023.

[8] K. Xin, Q. H. Zhan, and J. W. Lou, “A New Simple Sensorless Control Method for Switched Reluctance Motor Drives,” in *Proc. of 2005 International Conference on Electrical Machines and Systems*, Nanjing, China, Sep. 2005, vol. 1, pp. 594–598.

[9] E. Ofori, T. Husain, and Y. Sozer *et al*, “A Pulse Injection Based Sensorless Position Estimation Method for a Switched Reluctance Machine Over a Wide Speed Range,” in *Proc. of 2013 IEEE Energy Convers. Congr. and Expo.*, Denver, CO, USA, Sep. 2013, pp. 518–524.

[10] C. Gan, J. H. Wu, and S. Y. Yang *et al*, “Phase Current Reconstruction of Switched Reluctance Motors From DC-link Current under Double High-frequency Pulses Injection,” *IEEE Trans. on Ind. Electrons.*, vol. 62, no. 5, pp. 3265–3276, May 2015.

[11] D. X. Xiao, S. R. Filho, and G. L. Fang *et al*, “Position-sensorless Control of Switched Reluctance Motor Drives: A Review,” *IEEE Trans. Transport. Electrific.*, vol. 8, no. 1, pp. 1209–1227, Mar. 2022.

[12] S. J. Song, L. F. Ge, and Z. H. Zhang, “Accurate Position Estimation of SRM based on Optimal Interval Selection and Linear Regression Analysis,” *IEEE Trans. on Ind. Electrons.*, vol. 63, no. 6, pp. 3467–3478, Jun. 2016.

[13] L. F. Ge, H. H. Xu, and Z. C. Guo *et al*, “An Optimization-based Initial Position Estimation Method for Switched Reluctance Machines,” *IEEE*

Trans. on Power Electron., vol. 36, no. 11, pp. 13285–13292, Nov. 2021.

[14] J. H. Kim, and R. Y. Kim, "Online Sensorless Position Estimation for Switched Reluctance Motors Using Characteristics of Overlap Position based on Inductance Profile," *IET Electr. Power App.*, vol. 13, no. 4, pp. 456–462, Apr. 2019.

[15] J. Cai, Z. Y. Liu, and Y. Zeng, "Aligned Position Estimation Based Fault-tolerant Sensorless Control Strategy for SRM Drives," *IEEE Trans. on Power Electron.*, vol. 34, no. 8, pp. 7754–7762, Aug. 2019.

[16] J. H. Kim, and R. Y. Kim, "Sensorless Direct Torque Control Using the Inductance Inflection Point for a Switched Reluctance Motor," *IEEE Trans. on Ind. Electrons.*, vol. 65, no. 12, pp. 9336–9345, Dec. 2018.

[17] D. X. Xiao, J. Ye, and G. L. Fang *et al*, "Improved Feature-position-based Sensorless Control Scheme for SRM Drives based on Nonlinear State Observer at Medium and High Speeds," *IEEE Trans. on Power Electron.*, vol. 36, no. 5, pp. 5711–5723, May 2021.

[18] Z. F. Chen, H. Jing, and X. H. Wang *et al*, "General-purpose High-speed Position-sensorless Control of Switched Reluctance Motors Using Single-phase Adaptive Observer," *IEEE Trans. on Transport. Electrific.*, vol. 10, no. 3, pp. 5241–5249, Sept. 2024.

[19] Z. F. Chen, H. Jing, and X. H. Wang *et al*, "Selective Harmonic Elimination and Dynamic Enhancement in Magnetic-characteristic-free Sensorless Control of SRM Drives at High Speeds," *IEEE Trans. on Power Electron.*, vol. 39, no. 5, pp. 5339–55348, May 2024.

[20] F. Peng, J. Ye, and A. Emadi *et al*, "Position Sensorless Control of Switched Reluctance Motor Drives based on Numerical Method," *IEEE Trans. on Ind. Appl.*, vol. 53, no. 3, pp. 2159–2168, May-Jun. 2017.

[21] D. X. Lv, W. Ding, and Y. F. Wang *et al*, "Low-speed Sensorless Control of Switched Reluctance Motor Drives Using Random Pulse Injection for Noise Reduction," *IEEE Trans. on Trans. Electrific.*, vol. 11, no. 1, pp. 5005–5016, Feb. 2025.

[22] D. X. Xiao, J. Ye, and G. L. Fang *et al*, "A Regional Phase-locked Loop-based Low-speed Position-sensorless Control Scheme for General-purpose Switched Reluctance Motor Drives," *IEEE Trans. on Power Electron.*, vol. 37, pp. 5859–5873, May 2022.

[23] G. X. Li, Y. D. Chen, and A. Luo *et al*, "An Inertia Phase Locked Loop for Suppressing Sub-synchronous Resonance of Renewable Energy Generation System under Weak Grid," *IEEE Trans. on Power Syst.*, vol. 36, no. 5, pp. 4621–4631, Sept. 2021.

[24] G. X. Li, X. X. Bao, and X. Liu, "A Double-loop Inertia Phase-locked Loop with Antidisturbance Ability," *IEEE Trans. on Ind. Info.*, vol. 19, no. 4, pp. 5585–5592, Apr. 2023.

Zifeng Chen (Student Member, IEEE) received the B.S. degree in measurement and control technology and instrument from the Shenyang University of Technology, Shenyang, China, in 2018, and the M.S. degree in automation and control from Newcastle University, Newcastle upon Tyne, U.K., in 2020. He is currently working toward the Ph.D. degree in Sustainable Energy and Environment at The Hong Kong University of Science and Technology (Guangzhou), China. His research direction is motor drive and control.

Xijian Lin received the M.S. degree in electrical engineering from the School of Automation, Guangdong University of Technology, Guangzhou, China, in 2023. Currently, he is pursuing for the Ph.D. degree in Sustainable Energy and Environment at The Hong Kong University of Science and Technology (Guangzhou), China. His research interests include motor drive and battery management systems.

Huayu ji (Student Member, IEEE) received the B.S. in electrical engineering from Dalian Jiaotong University, Dalian, China, in 2019, and M. S. degree in electrical engineering from the South China University of Technology, Guangzhou, China, in 2022. He is currently working toward the Ph.D. degree in Sustainable Energy and Environment at The Hong Kong University of Science and Technology (Guangzhou), Guangzhou, China. His research interests include motor drives.

Zehua Li received the B.S. degree in electrical engineering and automation (power electronics and power drives) from Taiyuan University of Technology, Shanxi, China, in 2019, and M.S. degree in energy and power engineering from Xi'an Jiaotong University, Xi'an, China, in 2023. In addition, he has served as CEO and CTO of Energink Company since 2023 and is now a research assistant at Electric Propulsion & Energy Storage Lab. His current research interests include power converters and motor drivers for eVTOL applications

Hang Zhao (Member, IEEE) received the B.E. and M.E. degrees from Huazhong University of Science and Technology, Wuhan, China, and the Ph.D. degree from City University of Hong Kong, Hong Kong, all in electrical engineering in 2015, 2017, and 2021, respectively.

He was a Postdoctoral Research Fellow with The University of Hong Kong, Hong Kong in 2021. He is currently an Assistant Professor with the Robotics and Autonomous Systems Thrust, Systems Hub, The Hong Kong University of Science and Technology (Guangzhou), Guangzhou, China, and also an Affiliate Assistant Professor with the Department of Electronic and Computer Engineering, The Hong Kong University of Science and Technology, Hong Kong. His research interests include electric machines and drives, applications of motor drives in robots, and electrified transportation.

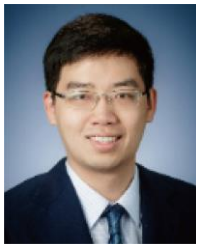

Dianxun Xiao (Member, IEEE) received the B.S. and M.S. degrees in electrical engineering from the Harbin Institute of Technology, Harbin, China, in 2016 and 2018, respectively, and the Ph.D. degree in electrical and computer engineering from McMaster University, Hamilton, ON, Canada, in 2021. He is currently an Assistant Professor with the Sustainable Energy and Environment Thrust, The Hong Kong University of Science and Technology (Guangzhou), Guangzhou, China, and also affiliated with The Hong Kong University of Science and Technology, HKSAR, China. Before that, he was a Postdoctoral Research Fellow with McMaster Automotive Resource Centre, McMaster University, Hamilton, ON, Canada, in 2021. He severs as an Associate Editor for IEEE Transactions on Transportation Electrification. He received the IEEE IAS The Myron Zucker Student-Faculty Grant in 2024. Research interests include permanent magnet synchronous motor drives, switched reluctance motor drives, high-power converters, and battery management systems for transportation electrification applications.